Modelling of transport phenomena in 3D GMAW of thick metals with V groove

2008 J. Phys. D: Appl. Phys. 41 065202

(http://iopscience.iop.org/0022-3727/41/6/065202)

IOP PUBLISHING JOURNAL OF PHYSICS D: APPLIED PHYSICS

J. Phys. D: Appl. Phys. **41** (2008) 065202 (10pp) doi:10.1088/0022-3727/41/6/065202

Modelling of transport phenomena in 3D GMAW of thick metals with V groove

J Hu[1] **and H L Tsai**[2]

[1] Department of Mechanical Engineering, University of Bridgeport, Bridgeport, CT 06604, USA
[2] Department of Mechanical and Aerospace Engineering, Missouri University of Science and Technology (formerly University of Missouri–Rolla), 1870 Miner Circle, Rolla, MO 65409, USA

Received 8 September 2007, in final form 23 January 2008
Published 22 February 2008
Online at stacks.iop.org/JPhysD/41/065202

Abstract

This paper analyses the dynamic process of groove filling and the resulting weld pool fluid flow in gas metal arc welding of thick metals with V groove. Filler droplets carrying mass, momentum, thermal energy and sulfur species are periodically impinged onto the workpiece. The complex transport phenomena in the weld pool, caused by the combined effect of droplet impingement, gravity, electromagnetic force, surface tension and plasma arc pressure, were investigated to determine the transient weld pool shape and distributions of velocity, temperature and sulfur species in the weld pool. It was found that the groove provides a channel which can smooth the flow in the weld pool, leading to poor mixing between the filler metal and the base metal.

(Some figures in this article are in colour only in the electronic version)

1. Introduction

Arc welding of thick metals is difficult because arc heat is easily diffused into the base metal, resulting in poor weld penetration. Welding of thick metals also leads to undesirable weld protrusion and excess reinforcement. Hence, arc welding of thick metals usually requires grooving and/or preheating of the base metal and, sometimes, multiple passes for very thick metals or metals with high thermal conductivity, such as aluminium alloys [1]. Depending upon weld joint geometries and other considerations, various grooving methods have been developed. In gas metal arc welding (GMAW), filler metals fill up the groove and provide thermal energy to heat and melt the base metal leading to the formation of a weld.

GMAW is a very complicated process involving many parameters, such as the power characteristics of the welding equipment, joint preparation, electrode type and size, shielding gas and physical and chemical properties of the base metals. Any of these parameters can significantly affect the formation of weld beads and ultimately the weld quality. As these parameters are coupled together and since GMAW involves a non-transparent metal and a high temperature plasma, it is rather difficult to experimentally isolate and identify the importance of each parameter. However, it is necessary to understand the role each parameter plays in transport phenomena occurring in the weld pool in order to optimize welding conditions and maximize weld quality. Mathematical modelling provides a convenient way to: (1) understand the physical phenomena involved in the welding process which may lead to the improvement in weld quality; (2) identify the key process parameters affecting weld quality; (3) investigate weld defects formation mechanisms; and (4) create innovative methods to improve weld quality. This paper is focused on the modelling of fundamental transport phenomena involved in a three-dimensional GMAW of a thick metal with a V groove.

Tsao and Wu [2] presented a two-dimensional stationary weld pool convection model in which the weld pool surface was assumed to be flat and mass transfer was not considered. Wang and Tsai [3] and Fan and Kovacevic [4, 5] investigated the dynamic impingement of droplets onto the weld pool and the solidification process in spot GMAW. Wang and Tsai [6] then continued to investigate the Marangoni effect caused by surface-active elements (SAEs) on weld pool mixing and weld penetration. Zhu *et al* [7] and Hu and Tsai [8, 9] further developed a comprehensive 2D GMAW model which can simulate the interactive coupling between the arc plasma, melting of the electrode, droplet formation, detachment, transfer and impingement onto the workpiece and weld pool dynamics. The comprehensive model was then used to study the effect of current on droplet generation and transfer in the arc [10, 11].

In a 3D moving GMAW, a simultaneous process, involving melting of the new solid base metal ahead of the molten pool and solidification of the weld pool on its tail, leads to a more complicated mixing process. Numerical modelling of a 3D moving GMAW is very limited and is frequently oversimplified. Using boundary-fitted coordinates, Kim and Na [12] presented a 3D quasi-steady heat and fluid flow analysis for the moving heat source of the GMAW process with free surface. However, impingement of droplets, the depression of the weld pool surface by arc pressure and Marangoni effects were not considered. Ushio and Wu [13] used a boundary-fitted non-orthogonal coordinate system to handle the largely deformed GMA weld pool surface and predicted the area and configuration of weld reinforcement. In their study, however, the heat delivered by metal transfer was approximated by an internal heat-generation term and the impact of droplets on the weld pool was considered to be a constant force acting on the surface. In other words, the impingement of droplets onto the weld pool was not actually simulated. Cao *et al* [14] used a commercial software package, FLOW-3D, to simulate a transient moving weld pool under the impact of droplet impingement; however, the droplet generation was not considered.

Hu *et al* [15] simulated a 3D moving GMAW in which droplets carrying mass, momentum, thermal energy and species are periodically impinged onto the weld pool. The interactions between droplet impingement, arc pressure, electromagnetic force and surface tension force were analysed. In their study, the dynamic impinging process and the distributions of velocity, temperature and sulfur concentration in the weld pool were calculated as a function of time.

In this paper, the 3D GMAW [15] model is extended to the case when welding a thick metal with V groove, using the volume of fluid (VOF) technique [16] and the continuum formulation [17]. As in previous studies [6], sulfur is selected as the SAE element which not only significantly changes the magnitude of surface tension in the weld pool but also serves as an indicator of the degree of mixing between filler metal and base metal. The VOF technique can handle the transient deformed weld pool surface caused by droplet impingement and arc pressure. The continuum formulation can handle the fusion and solidification, the liquid region, mushy zone and solid region simultaneously, providing a facility to track the moving phase-change boundary. In this study, as we will focus on weld pool dynamics, and in order to save computational time, the droplet generation and the arc plasma are not calculated. Instead, typical droplet conditions, including size, impinging velocity, temperature and frequency, are assumed based on the previous studies [8–11]. The plasma arc is assumed to be a Gaussian profile. Note these assumptions should not change the fundamental characteristics of the droplet impinging process and the resulting weld pool dynamics to be studied in this study.

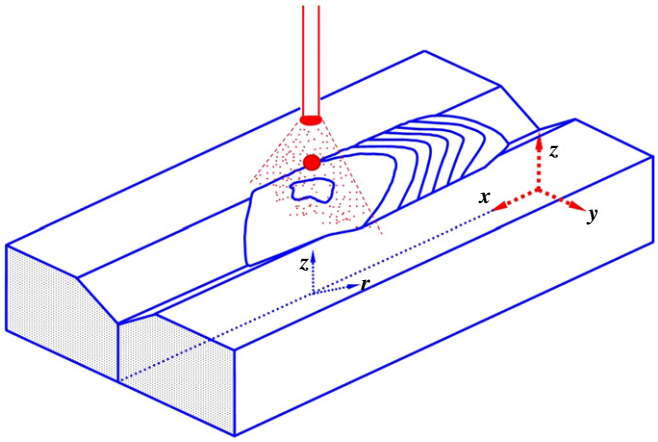

Figure 1. Schematic sketch of a moving GMAW system for a thick plate with groove: x–y–z is a stationary Cartesian coordinate system and r–z is a cylindrical coordinate system moving with the main arc.

2. Mathematical formulation

2.1. Governing equations

Figure 1 is a schematic sketch of a moving GMAW for a thick plate with V groove. The 3D x–y–z coordinate system is fixed to the stationary base metal, while the 2D r–z cylindrical coordinate system moves with the arc centre. In GMAW, the arc energy is split into two parts: one to melt the electrode and generate droplets and the other to directly heat the base metal. Hence, in addition to the thermal energy, mass and momentum carried by the droplets, arc heat flux simultaneously impacts onto the base metal. Droplets, containing a different sulfur concentration from that of the base metal, are assumed to periodically impinge onto the base metal in the negative z-direction, while they move at the same velocity along the x-direction as the arc. For convenience, the mathematical formulation given below is valid for both the base metal and the liquid droplets. However, the temperature and concentration are assumed to be constant for droplets. Once a droplet reaches the free surface, it is immediately considered to be part of the base metal and then the exchange of momentum, energy and species between the droplet and the weld pool occurs.

The differential equations governing the conservation of mass, momentum, energy and species based on the continuum formulation given by Diao and Tsai [17] are modified and employed in this study and are given below.

(1) Continuity:

$$\frac{\partial}{\partial t}(\rho) + \nabla \cdot (\rho \boldsymbol{V}) = 0. \tag{1}$$

(2) Momentum:

$$\frac{\partial}{\partial t}(\rho u) + \nabla \cdot (\rho \boldsymbol{V} u) = \nabla \cdot \left(\mu_{\mathrm{l}} \frac{\rho}{\rho_{\mathrm{l}}} \nabla u\right) - \frac{\partial p}{\partial x} - \frac{\mu_{\mathrm{l}}}{K} \frac{\rho}{\rho_{\mathrm{l}}} (u - u_{\mathrm{s}}) - \frac{C\rho^2}{K^{1/2}\rho_{\mathrm{l}}} |u - u_{\mathrm{s}}|(u - u_{\mathrm{s}}) - \nabla \cdot (\rho f_{\mathrm{s}} f_{\mathrm{l}} \boldsymbol{V}_{\mathrm{r}} u_{\mathrm{r}}) + \nabla \cdot \left(\mu_{\mathrm{l}} u \nabla \left(\frac{\rho}{\rho_{\mathrm{l}}}\right)\right) + \boldsymbol{J} \times \boldsymbol{B}|_x, \tag{2}$$

$$\frac{\partial}{\partial t}(\rho v) + \nabla \cdot (\rho \boldsymbol{V} v) = \nabla \cdot \left(\mu_l \frac{\rho}{\rho_l} \nabla v\right) - \frac{\partial p}{\partial y} - \frac{\mu_l}{K}\frac{\rho}{\rho_l}(v - v_s) - \frac{C\rho^2}{K^{1/2}\rho_l}|v - v_s|(v - v_s) - \nabla \cdot (\rho f_s f_l \boldsymbol{V}_r v_r) + \nabla \cdot \left(\mu_l v \nabla \left(\frac{\rho}{\rho_l}\right)\right) + \boldsymbol{J} \times \boldsymbol{B}|_y, \quad (3)$$

$$\frac{\partial}{\partial t}(\rho w) + \nabla \cdot (\rho \boldsymbol{V} w) = \rho g + \nabla \cdot \left(\mu_l \frac{\rho}{\rho_l} \nabla w\right) - \frac{\partial p}{\partial z} - \frac{\mu_l}{K}\frac{\rho}{\rho_l}(w - w_s) - \frac{C\rho^2}{K^{1/2}\rho_l}|w - w_s|(w - w_s) - \nabla \cdot (\rho f_s f_l \boldsymbol{V}_r w_r) + \nabla \cdot \left(\mu_l w \nabla \left(\frac{\rho}{\rho_l}\right)\right) + \rho g(\beta_T(T - T_0) + \beta_s(f_l^\alpha - f_{l,0}^\alpha)) + \boldsymbol{J} \times \boldsymbol{B}|_z + F_{drag}. \quad (4)$$

(3) Energy:

$$\frac{\partial}{\partial t}(\rho h) + \nabla \cdot (\rho \boldsymbol{V} h) = \nabla \cdot \left(\frac{k}{c_s} \nabla h\right) + \nabla \cdot \left(\frac{k}{c_s} \nabla (h_s - h)\right) - \nabla \cdot (\rho(\boldsymbol{V} - \boldsymbol{V}_s)(h_l - h)). \quad (5)$$

(4) Species:

$$\frac{\partial}{\partial t}(\rho f^\alpha) + \nabla \cdot (\rho \boldsymbol{V} f^\alpha) = \nabla \cdot (\rho D \nabla f^\alpha) + \nabla \cdot (\rho D \nabla (f_l^\alpha - f^\alpha)) - \nabla \cdot (\rho(\boldsymbol{V} - \boldsymbol{V}_s)(f_l^\alpha - f^\alpha)). \quad (6)$$

The above six equations are similar to those given in [17], except the electromagnetic force (or Lorentz force), $\boldsymbol{J} \times \boldsymbol{B}$, where $\boldsymbol{J}$ is the electric current density vector and $\boldsymbol{B}$ is the magnetic flux vector. As the assumptions to derive the equations and the physical meanings of their terms are given by Diao and Tsai [17], they will not be repeated here. The electromagnetic force is assumed to be independent of the properties of the fluid flow in the weld pool, and the x, y and z components will be calculated first, as discussed next, before the velocity is calculated. The second to the last term in equation (4) is the buoyancy force which is based on the Boussinesq approximation for natural convection caused by both thermal and solutal convections.

In equations (1)–(6), the continuum density, specific heat, thermal conductivity, mass diffusivity, solid mass fraction, liquid mass fraction, velocity, enthalpy and mass fraction of constitute are defined as follows:

$$\rho = g_s\rho_s + g_l\rho_l, \quad c = f_s c_s + f_l c_l, \quad k = g_s k_s + g_l k_l, \quad D = f_s D_s + f_l D_l, \quad f_s = \frac{g_s\rho_s}{\rho}, \quad f_l = \frac{g_l\rho_l}{\rho}, \quad \boldsymbol{V} = f_s \boldsymbol{V}_s + f_l \boldsymbol{V}_l, \quad h = h_s f_s + h_l f_l, \quad f^\alpha = f_s f_s^\alpha + f_l f_l^\alpha \quad (7)$$

where g_s and g_l are the volume fractions of the solid and liquid phases, respectively. If the phase specific heats are assumed constant, the phase enthalpy for the solid and the liquid can be expressed as

$$h_s = c_s T, \quad h_l = c_l T + (c_s - c_l)T_s + H, \quad (8)$$

where H is the latent heat of fusion of the alloy.

The assumption of the permeability function in the mushy zone requires the consideration of the growth morphology specific to the alloy under study. In this study, the permeability function analogous to the fluid flow in porous media is assumed employing the Carman–Kozeny equation [18, 19],

$$K = \frac{g_l^3}{c_1(1 - g_l)^2}, \quad c_1 = \frac{180}{d^2}, \quad (9)$$

where d is proportional to the dendrite dimension, which is assumed to be a constant and is on the order of 10^{-2} cm. The inertial coefficient, C, can be calculated from [20]

$$C = 0.13 g_l^{-3/2}. \quad (10)$$

2.2. Tracking of solid–liquid interface

The solid/liquid phase-change is handled by the continuum formulation [17]. The third, fourth and fifth terms in the right-hand side of equations (2) and (3), and similar terms in equation (4), vanish in the solid region because $u = u_s = v = v_s = w = w_s = 0$ and $f_l = 0$ for the solid phase. For the liquid region, since K goes to infinity due to $g_l = 1$ in equation (9) and $f_s = 0$, all these terms also vanish. These terms are only valid in the mushy zone where $0 < f_l < 1$ and $0 < f_s < 1$. Therefore, the liquid region, the mushy zone and the solid region can be handled by the same equations. Also, in GMAW, as the arc heat flux is rather concentrated and the solidification time is very short (as compared with, for example, a casting process), it is expected that the mushy zone in the base metal is very small, and the solid phase velocity is assumed to be zero in the mushy zone. During the fusion and solidification process, latent heat is absorbed or released in the mushy zone. By using enthalpy, conduction in the solid region, conduction and convection in the liquid region and mushy zone, the absorption and release of latent heat are all handled by the same equation, equation (5).

2.3. Tracking of free surfaces

The algorithm of VOF is used to track the dynamic geometry of the free surface [16]. The fluid configuration is defined by a VOF function, *F(x, y, z, t)*, which tracks the location of the free surface. This function represents the VOF per unit volume and satisfies the following conservation equation:

$$\frac{\mathrm{d}F}{\mathrm{d}t} = \frac{\partial F}{\partial t} + (\boldsymbol{V} \cdot \nabla)F = 0. \quad (11)$$

When averaged over the cells of a computing mesh, the average value of F in a cell is equal to the fractional volume of the cell occupied by the fluid (i.e. metal in this study). A unit value of F corresponds to a cell full of fluid, whereas a zero value indicates a cell containing no fluid. Cells with F values between zero and one are partially filled with fluid and identified as surface cells.

2.4. Boundary conditions

The boundary conditions for the solution of equation (1) through equation (6) are given below.

2.4.1. Normal to the local free surface. For cells containing free surface, that is, cells that contain fluid but have one or more empty neighbours, the following pressure conditions must be satisfied [16]:

$$p = p_{\mathrm{v}} + \gamma\kappa, \tag{12}$$

where p is the pressure at the free surface in a direction normal to the local free surface and p_{v} is the vapour pressure or any other applied external pressure acting on the free surface, which, in this study, is the plasma arc pressure. The plasma arc pressure is assumed to have a radial distribution of the following form [13]:

$$p_{\mathrm{v}} = P_{\max}\exp\left(-\frac{r^2}{2\sigma_{\mathrm{p}}^2}\right), \tag{13}$$

where $P_{\max}$ is the maximum arc pressure at the arc centre, r is the distance from the arc centre ($x = x_{\mathrm{a}}$, $y = 0$) and σ_{p} is the arc pressure distribution parameter. In equation (12), κ is the free surface curvature given by [16]

$$\kappa = -\left[\nabla\cdot\left(\frac{\vec{n}}{|\vec{n}|}\right)\right] = \frac{1}{|\vec{n}|}\left[\left(\frac{\vec{n}}{|\vec{n}|}\cdot\nabla\right)|\vec{n}| - (\nabla\cdot\vec{n})\right], \tag{14}$$

where $\vec{n}$ is a normal vector to the local surface, which is the gradient of the VOF function

$$\vec{n} = \nabla F. \tag{15}$$

2.4.2. Tangential to the local free surface. The temperature and sulfur concentration dependent Marangoni shear stress at the free surface in a direction tangential to the local free surface is given by

$$\tau_{\vec{s}} = \mu_{\mathrm{l}}\frac{\partial(\boldsymbol{V}\cdot\vec{s})}{\partial\vec{n}} = \frac{\partial\gamma}{\partial T}\frac{\partial T}{\partial\vec{s}} + \frac{\partial\gamma}{\partial f^{\alpha}}\frac{\partial f^{\alpha}}{\partial\vec{s}}, \tag{16}$$

where $\vec{s}$ is a tangential vector to the local surface. Surface tension γ for a pseudo-binary Fe–S system as a function of temperature, T, and the sulfur concentration, f^{α}, is given by [21]

$$\begin{aligned}\gamma &= 1.943 - 4.3\times10^{-4}(T-1723)\\ &\quad -RT\times1.3\times10^{-8}\\ &\quad \times\ln\left(1+0.00318\,f^{\alpha}\exp\left(\frac{1.66\times10^{8}}{RT}\right)\right),\end{aligned} \tag{17}$$

where R is the gas constant.

2.5. Top surface

At the moving arc centre, in addition to droplet impingement, arc heat flux also impacts on the base metal. As the arc heat flux is rather concentrated, the heat flux is assumed to impact perpendicularly on the base metal (i.e. neglecting the inclination nature of current and heat flux [8]). Hence, the temperature and concentration boundary conditions at the top surface of the base metal are

$$k\frac{\partial T}{\partial z} = \frac{\eta(1-\eta_{\mathrm{d}})I\,u_{\mathrm{w}}}{2\pi\sigma_q^2}\exp\left(-\frac{r^2}{2\sigma_q^2}\right) - q_{\mathrm{conv}} - q_{\mathrm{radi}} - q_{\mathrm{evap}}, \tag{18}$$

$$\frac{\partial f^{\alpha}}{\partial z} = 0, \tag{19}$$

where I is the welding current, η is the arc thermal efficiency, η_{d} is the ratio of droplet thermal energy to the total arc energy, u_{w} is the arc voltage and σ_q is the arc heat flux distribution parameter. The heat loss due to convection, radiation and evaporation can be written as

$$\begin{aligned}&q_{\mathrm{conv}} = h_{\mathrm{c}}(T - T_{\infty}), \qquad q_{\mathrm{radi}} = \sigma\varepsilon(T^4 - T_{\infty}^4),\\ &q_{\mathrm{evap}} = W H_{\mathrm{v}},\end{aligned} \tag{20}$$

where h_{c} is the convective heat transfer coefficient, σ is the Stefan–Boltzmann constant, ε is the radiation emissivity, H_{v} is the latent heat for the liquid–vapour phase-change and W is the melt mass evaporation rate. For a metal such as steel, W can be written as [22]

$$\log(W) = A_{\mathrm{v}} + \log P_{\mathrm{atm}} - 0.5\log T, \tag{21}$$

$$\log P_{\mathrm{atm}} = 6.121 - \frac{18836}{T}, \tag{22}$$

where A_{v} is a constant taken as 0.52 and P_{atm} is the ambient pressure.

2.5.1. Symmetrical $y = 0$ plane.

$$\begin{aligned}&\frac{\partial u}{\partial y} = 0, \qquad v = 0, \qquad \frac{\partial w}{\partial y} = 0, \qquad \frac{\partial T}{\partial y} = 0,\\ &\frac{\partial f^{\alpha}}{\partial y} = 0.\end{aligned} \tag{23}$$

2.5.2. Other surfaces

$$\begin{aligned}&-k\frac{\partial T}{\partial\vec{n}} = q_{conv}, \qquad u = 0, \qquad v = 0, \qquad w = 0,\\ &\frac{\partial f^{\alpha}}{\partial\vec{n}} = 0,\end{aligned} \tag{24}$$

where $\vec{n}$ can be either x-, y- or z-direction.

2.6. Electromagnetic force

In each of equations (2) through (4), there is a term caused by the electromagnetic force that should be calculated first before the calculation of velocity. Assuming the electric field is quasi-steady-state and the electrical conductivity is constant, the scalar electric potential, ϕ, satisfies the following Maxwell equation in the local r–z coordinate system [8]:

$$\nabla^2\phi = \frac{1}{r}\frac{\partial}{\partial r}\left(r\frac{\partial\phi}{\partial r}\right) + \frac{\partial^2\phi}{\partial z^2} = 0. \tag{25}$$

The required boundary conditions for the solution of equation (25) are

$$-\sigma_e \frac{\partial \phi}{\partial z} = \frac{I}{2\pi\sigma_c^2} \exp\left(-\frac{r^2}{2\sigma_c^2}\right) \text{ at the top surface,} \tag{26}$$

$$\frac{\partial \phi}{\partial z} = 0 \qquad \text{at } z = 0, \tag{27}$$

$$\frac{\partial \phi}{\partial r} = 0 \qquad \text{at } r = 0, \tag{28}$$

$$\phi = 0 \qquad \text{at } r = 10\sigma_c \tag{29}$$

where σ_e is the electrical conductivity and σ_c is the arc current distribution parameter. After the distribution of electrical potential is solved, current density in the r- and z-directions can be calculated via

$$J_r = -\sigma_e \frac{\partial \phi}{\partial r}, \qquad J_z = -\sigma_e \frac{\partial \phi}{\partial z}. \tag{30}$$

The self-induced azimuthal magnetic field is derived from Ampere's law through [8]

$$B_\theta = \frac{\mu_0}{r} \int_0^r J_z r \, \mathrm{d}r, \tag{31}$$

where μ_0 is the magnetic permeability. Finally, the three components of electromagnetic force in equations (2)–(4) are calculated via

$$\boldsymbol{J} \times \boldsymbol{B}|_x = -B_\theta J_z \frac{x - x_a}{r}, \qquad \boldsymbol{J} \times \boldsymbol{B}|_y = -B_\theta J_z \frac{y}{r},$$
$$\boldsymbol{J} \times \boldsymbol{B}|_Z = B_\theta J_r. \tag{32}$$

3. Numerical method

Finite difference conventions follow that of the MAC scheme [23] in which x-, y- and z-velocity components are located at cell face centres on lines of constants x, y and z, respectively, and the pressure, VOF function, temperature and concentration are located at cell centres. The numerical procedures used in this study for the aforementioned governing differential equations are briefly discussed in the following.

1. The momentum differential equations are cast into the general format suggested by Patankar [24]:

$$\frac{\partial(\rho \boldsymbol{V})}{\partial t} + \nabla \cdot (\rho \boldsymbol{V}\boldsymbol{V}) = \nabla \cdot \boldsymbol{\tau} + S_\phi, \tag{33}$$

where $\boldsymbol{\tau}$ is the viscous stress tensor and S_ϕ is the source term, which includes the pressure gradient, Darcy's function, the relative phase motion, electromagnetic force, gravitational force and buoyancy force in the momentum equations. Equation (33) is solved in the finite difference form with a two-step projection method involving the time discretization of momentum equations (2)–(4). The step one equation is

$$\frac{\tilde{\boldsymbol{V}} - \boldsymbol{V}^n}{\delta t} = -\nabla \cdot (\boldsymbol{V}\boldsymbol{V})^n + \frac{1}{\rho^n} \nabla \cdot \boldsymbol{\tau}^n + \frac{1}{\rho^n} S_\phi^n, \tag{34}$$

where the velocity field $\tilde{\boldsymbol{V}}$ is explicitly computed from incremental changes in the field $\boldsymbol{V}^n$ resulting from advection, viscosity and the source term. In step two, the velocity field $\tilde{\boldsymbol{V}}$ is projected onto a zero-divergence vector field $\boldsymbol{V}^{n+1}$ using the following two equations:

$$\frac{\boldsymbol{V}^{n+1} - \tilde{\boldsymbol{V}}}{\delta t} = -\frac{1}{\rho^n} \nabla p^{n+1}, \tag{35}$$

$$\nabla \cdot \boldsymbol{V}^{n+1} = 0. \tag{36}$$

These two equations can be combined into a single Poisson equation for the pressure, which is solved by the incomplete Cholesky conjugate gradient (ICCG) solution technique [25]:

$$\nabla \cdot \left[\frac{1}{\rho^n} \nabla p^{n+1}\right] = \frac{\nabla \cdot \tilde{\boldsymbol{V}}}{\delta t}. \tag{37}$$

2. Equation (11) is initiated by defining an immediate $\tilde{F}$:

$$\tilde{F} = F^n - \delta t \nabla \cdot (\boldsymbol{V} F^n). \tag{38}$$

It can be completed with a divergence correction to get F^{n+1} for the new fluid domain:

$$F^{n+1} = \tilde{F} + \delta t (\nabla \cdot \boldsymbol{V}) F^n. \tag{39}$$

3. The equations of energy, species and Maxwell are solved explicitly to determine the distribution of temperature, concentration and electromagnetic field, respectively. Equation (7) is then used to update the liquid-fraction, material properties, etc.
4. Finally, at a certain period of time, a new droplet with given diameter, temperature and concentration is produced and the surface boundary condition is imposed on this new droplet. Repetition of the aforementioned steps produces the solution until the time is out.

Since the governing equations are valid in the regions of liquid, solid and mushy zone, there is no need to track the geometrical shape and the extent of each region. Hence, a fixed-grid system is used in the numerical calculation. Due to symmetry of the x–z plane of the domain, a grid system of points ($408 \times 51 \times 62$) was used in the actual calculation to simulate half of the computational domain. As the weld pool moves in the welding direction, an adaptive grid system is employed, having finer grids in the weld pool. The finer grids concentrating on and around the weld pool move with the weld pool as welding proceeds. However, in order to enhance readability, only a part of the grid points is used for all velocity plots that will be presented below. The average time step is 10^{-4} s and the smallest time step is 10^{-5} s which occurs when the droplet impinges on the weld pool.

4. Results and discussion

The flow pattern, distributions of temperature and sulfur concentration and the final weld pool penetration for a moving GMAW for 304 stainless steels were calculated. In order to

simulate a realistic welding process, typical welding conditions were selected as a forced input. As in previous studies [6], to examine the effect of surface tension on the weld pool fluid flow, sulfur was selected as the SAE. The welding conditions and material properties of both base metal and droplets used in the computation are summarized in table 1. The droplet is assumed to be spherical, and based on the welding conditions and the results from our previous studies on droplet generation [8–11], the following droplet conditions are selected in this study to represent a globular transfer mode: droplet diameter (1.85 mm), droplet generation frequency (24 Hz), droplet impinging velocity (30 cm s^{-1}) and droplet temperature (2500 K). Among the tremendous results obtained from the simulation, only some selected representative results will be presented below.

4.1. Interaction between filler droplets and weld pool

The base metal is heated by the arc and by the thermal energy carried by droplets. As more droplets enter the groove, a weld pool is gradually formed and becomes larger with time. Depending upon the welding speed, the wire size (i.e. droplet diameter) and the wire feeding speed (i.e. the number of droplets per second), the groove can be completely filled up by the filler metal. To avoid end effects, the first droplet impinges onto the base metal at $X = 5$ mm, figure 1. Figure 2 is a partial view of the three-dimensional mesh and filler metal deposition at $t = 4.300$ s. The shape of the weld bead in the groove can be clearly seen, showing some distinct ripples in the solidified weld surface and the crater, both of which are very similar to an actual welding. The formation of ripples at the surface of the solidified weld bead is caused by a combined effect of droplet impingement, weld pool dynamics and solidification and has been discussed previously for welding without a groove [15].

Although droplet impinging is a dynamic process, a quasi-steady-state of the weld pool can be reached after $X = 15$ mm, as shown in figure 2. In order to explain the transport phenomena occurring in the weld pool, a sequence of four figures during one typical periodic impinging process are selected and discussed below.

4.1.1. Side view of the impinging process. Figure 3 shows a side view of a droplet impinging process onto the weld pool during one typical periodic cycle and the isotherm curves at different times. Figures 4 and 5 are, respectively, the corresponding velocity and sulfur concentration distributions in the weld pool.

At $t = 4.305$ s, a new droplet reaches the weld pool at the arc centre, figure 3. It has a vertical speed of -30 cm s^{-1} and a horizontal speed of 0.7 cm s^{-1}, which is the same as the welding speed. As shown in the figure, the isotherm curve of 1725 K is the liquidus line, and the 1670 K curve represents the solidus line. It is seen that the mushy zone is very small, which is consistent with our previous assumption. Outside the solidus line, the temperature distribution is quite regular since there is no heat convection in the solid metal. Inside the liquidus line is the weld pool where the distributions of temperature, velocity and sulfur concentration are complex.

Table 1. Thermophysical properties of 304 stainless steel and welding conditions.

Nomenclature	Symbol	Value
Specific heat of solid phase	c_s	700 J kg^{-1} K^{-1}
Specific heat of liquid phase	c_l	780 J kg^{-1} K^{-1}
Mass diffusion coefficient of solid phase	D_s	$\cong 0$
Mass diffusion coefficient of liquid phase	D_l	3×10^{-5} cm^2 s^{-1}
Thermal conductivity of solid phase	k_s	22 W m^{-1} K^{-1}
Thermal conductivity of liquid phase	k_l	22 W m^{-1} K^{-1}
Density of solid phase	ρ_s	7200 kg m^{-3}
Density of liquid phase	ρ_l	6900 kg m^{-3}
Thermal expansion coefficient	β_T	4.95×10^{-5} K^{-1}
Solutal expansion coefficient	β_s	-2.0
Radiation emissivity	ε	0.4
Dynamic viscosity	μ_l	0.006 kg m^{-1} s^{-1}
Latent heat of fusion	H	2.47×10^5 J kg^{-1}
Magnetic permeability	μ_0	1.26×10^{-6} H m^{-1}
Solidus temperature	T_s	1670 K
Liquidus temperature	T_l	1725 K
Reference temperature	T_0	293 K
Ambient temperature	T_∞	293 K
Convective heat transfer coefficient	h_c	80 W m^{-2} K^{-1}
Latent heat of vaporization	H_v	7.34×10^6 J kg^{-1}
Initial base metal temperature	T_b	293 K
Thickness of base metal	H_b	8.1 mm
Width of base metal	W_b	30.0 mm
Length of base metal	L_b	300.0 mm
Groove depth	D_g	3.1 mm
Groove angle	θ_g	90°
Initial base metal sulfur concentration	f_b^α	100 ppm
Electrical conductivity	σ_e	7.14×10^5 Ω^{-1} m^{-1}
Welding voltage	u_w	20 V
Welding current	I	240 A
Arc heat flux distribution parameter	σ_q	2.50×10^{-3} m
Arc current distribution parameter	σ_c	2.50×10^{-3} m
Welding speed	V_a	7.0 mm s^{-1}
Arc thermal efficiency	η	70%
Ratio of droplet thermal energy to total arc energy	η_d	35%
Droplet diameter	D_d	1.85 mm
Droplet frequency	F_d	24 Hz
Droplet impinging velocity	V_d	30 cm s^{-1}
Initial droplet temperature	T_d	2500 K
Initial droplet sulfur concentration	f_d^α	300 ppm
Maximum plasma arc pressure	P_{max}	100.0 Pa
Plasma arc pressure distribution parameter	σ_p	5.0×10^{-3} m

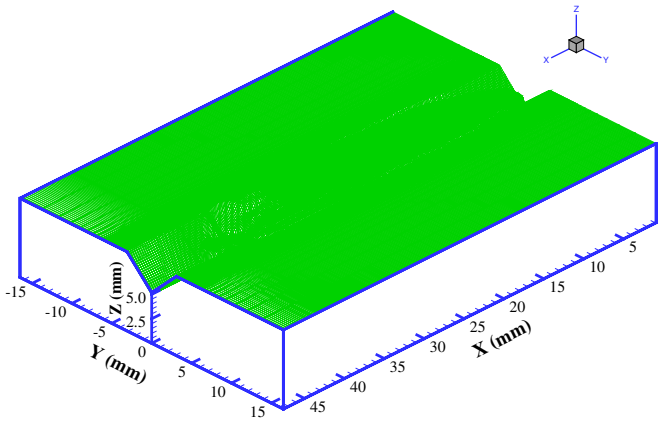

Figure 2. Partial view of a three-dimensional mesh system and weld deposition at $t = 4.300$ s.

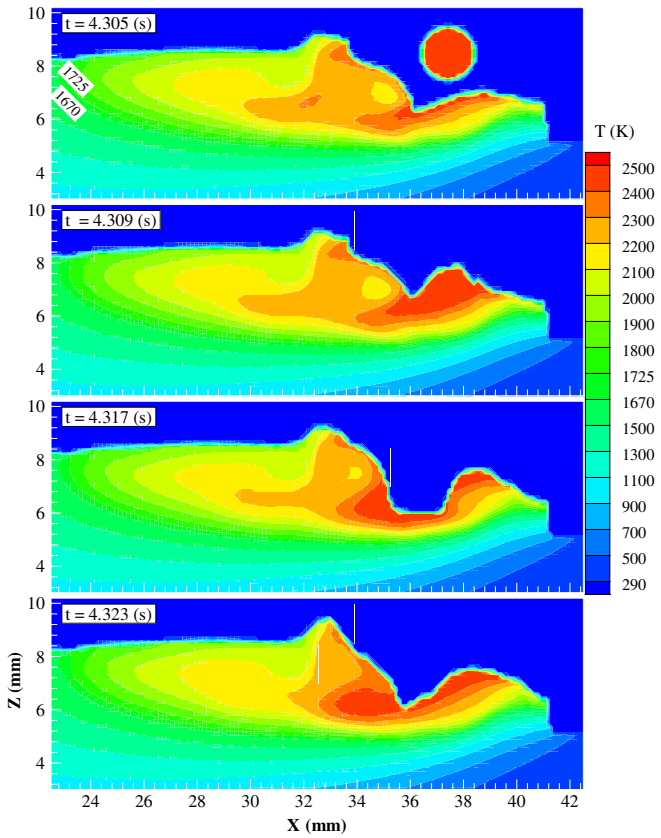

Figure 3. A typical sequence showing the impinging process, weld pool dynamics and temperature distribution in the plane $Y = 0$ (side view).

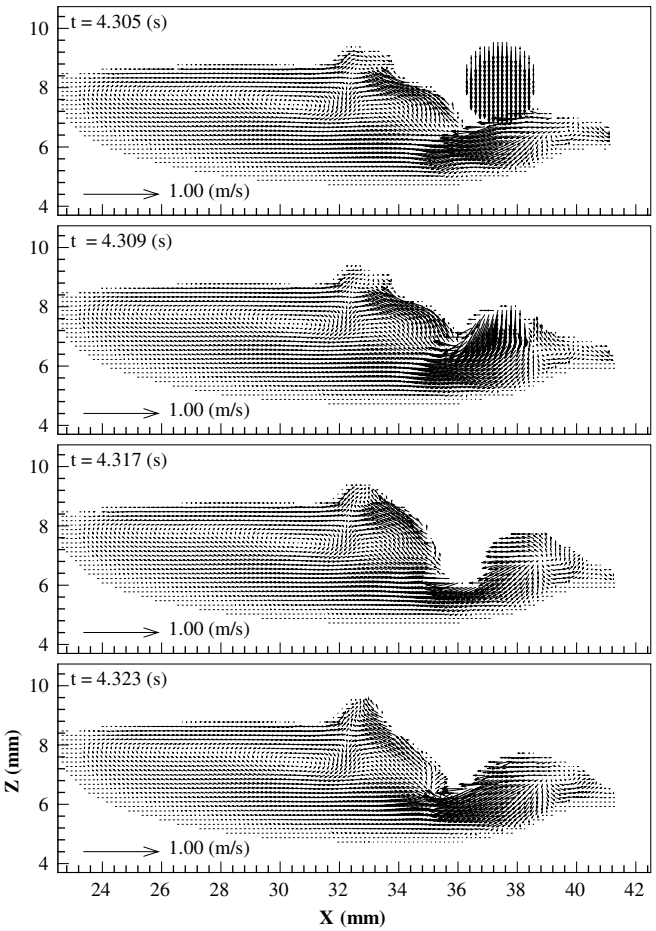

Figure 4. The corresponding velocity profiles as shown in figure 3.

As shown in figures 3 and 5, there are several 'spots' with either higher temperatures or sulfur concentrations; some are near the arc centre at the weld pool surface and others are inside the weld pool. The non-uniform temperature and sulfur distributions can be explained by using the flow pattern in figure 4. As shown in figure 4, when a droplet impinges onto the base metal, part of the droplet fluid sprawls forward to the right-hand side and up to $X = 40.0$ mm. A portion of the weld pool ahead of the arc centre can also be seen in figure 2. On the other hand, part of the droplet fluid flows backwards to the left-hand side at higher velocities, as compared with fluid on the right-hand side. The left-hand flow is split into two flows: one turns upwards to the surface and the other is along the bottom of the groove. As the droplet has the highest temperature and contains the highest sulfur, the left-hand flow leads to higher temperatures and sulfur concentrations at the surface near the arc centre and inside the weld pool. The upturn flow at the weld pool collides with a flow from the left, creating a 'bump' at $X = 33.0$ mm.

There are three forces pulling the surface fluid between $X = 33.0$ mm and $X = 36.0$ mm outwards from the arc centre. First, the impinging droplet pushes the liquid outwards from the arc centre. Second, the arc pressure (which is assumed to have a radial distribution about the arc centre, equation (13)) also produces the outward force at the surface close to the arc centre. Finally, the Marangoni shear force makes an important contribution to this flow pattern. From the arc centre to $X = 33.0$ mm, as the surface temperature is above 2300 K and decreases outwards (figure 3) and the surface sulfur concentration is above 250 ppm (figure 4), the temperature coefficient of surface tension is negative [15]. Therefore, the Marangoni force is outwards, creating an outward flow away from the arc centre.

At the same time, the surface fluid between the tail edge of the weld pool and $X = 32.0$ mm flows toward the arc centre. Since the surface temperature is below 2000 K and surface sulfur concentration is about 200 ppm, the temperature

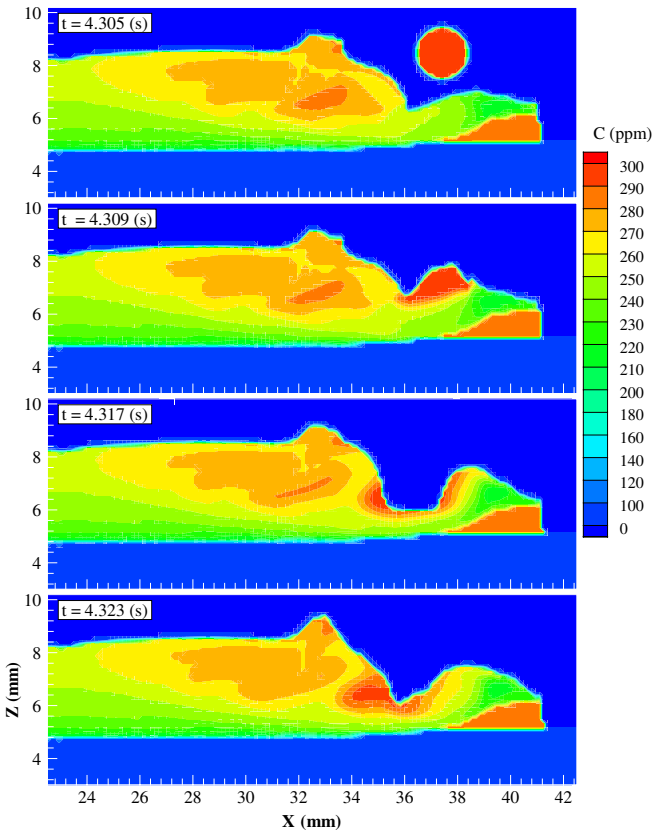

Figure 5. The corresponding sulfur concentration distribution as shown in figure 3.

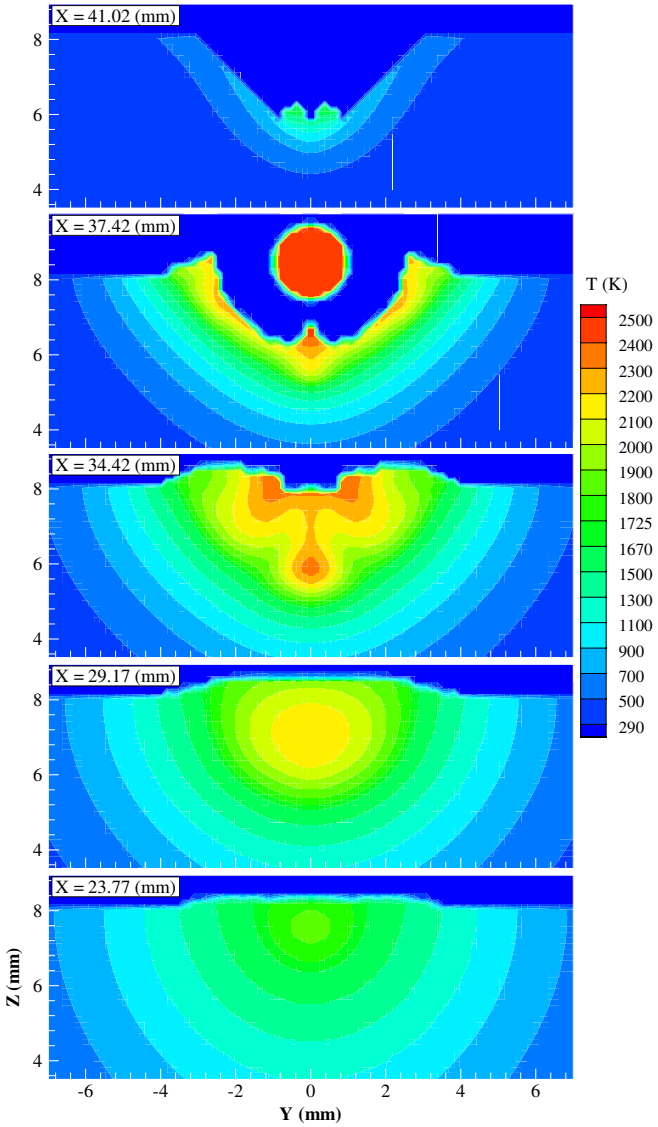

Figure 6. Cross-sectional temperature distributions at different X locations at $t = 4.305$ s (front view).

coefficient of surface tension is positive [15] and, as a result, the Marangoni force is towards the arc centre. Hence, the two surface fluid flows with opposite directions collide at $X = 33.0$ mm, pushing some of the fluid upwards and the rest downwards. This downward fluid flow combines with the fluid flow along the bottom, as mentioned previously, producing a large clockwise vortex centred at $X = 31$ mm.

By looking at the movement of 'dark spots' in figures 3 and 5 at different times, it is clearly seen that these spots are consistent with the movement of fluid from the droplet in figure 4. Due to droplet impingement at $t = 4.309$ s, free surface is deformed and a 'crater' is formed at $t = 4.317$ s. At $t = 4.323$ s, the crater becomes smaller since the surrounding fluid tends to flatten it. Depending upon the droplet size, drop frequency, welding speed, the crater can be opened and closed up in a certain frequency. Under the welding conditions used in this study, it appears that the crater's size can change with time but will not be completely closed up. As seen in figure 4, the flow patterns in the weld pool are very similar at different times except near the arc centre in which the flow is caused mainly by droplet impingement.

4.1.2. Front view of the impinging process. Figure 6 is the front view of the temperature distribution at different positions along the welding direction at $t = 4.305$ s corresponding to figures 3–5. Figures 7 and 8 are, respectively, the corresponding velocity and sulfur concentration distributions of figure 6.

At $X = 41.02$ mm, 3.6 mm ahead of the arc centre, the base metal at both sides of the groove has already been heated by arc heat. At the bottom of the groove, there is some mass overflow from the weld pool. This part of the metal cooled by the base metal is almost in a solid state. At $X = 37.42$ mm, which is the arc centre, a new droplet with a temperature of 2500 K and sulfur concentration of 300 ppm appears inside the groove and is ready to impinge onto the weld pool. At this location, melting of the base metal is limited and the liquid layer is thin, as can be seen in figures 7 and 8. The velocity distribution in this thin liquid layer is complicated. The high sulfur concentration near the top portion of the groove is caused by the spatter of the droplets containing the highest sulfur, figure 8.

At $X = 34.42$ mm, which is 3 mm behind the arc centre, the groove is already filled by the mass of droplets. There are two areas with the highest temperature and sulfur concentration. One is at the surface around the arc centre caused by the outward flow of the impinged droplet fluid, as

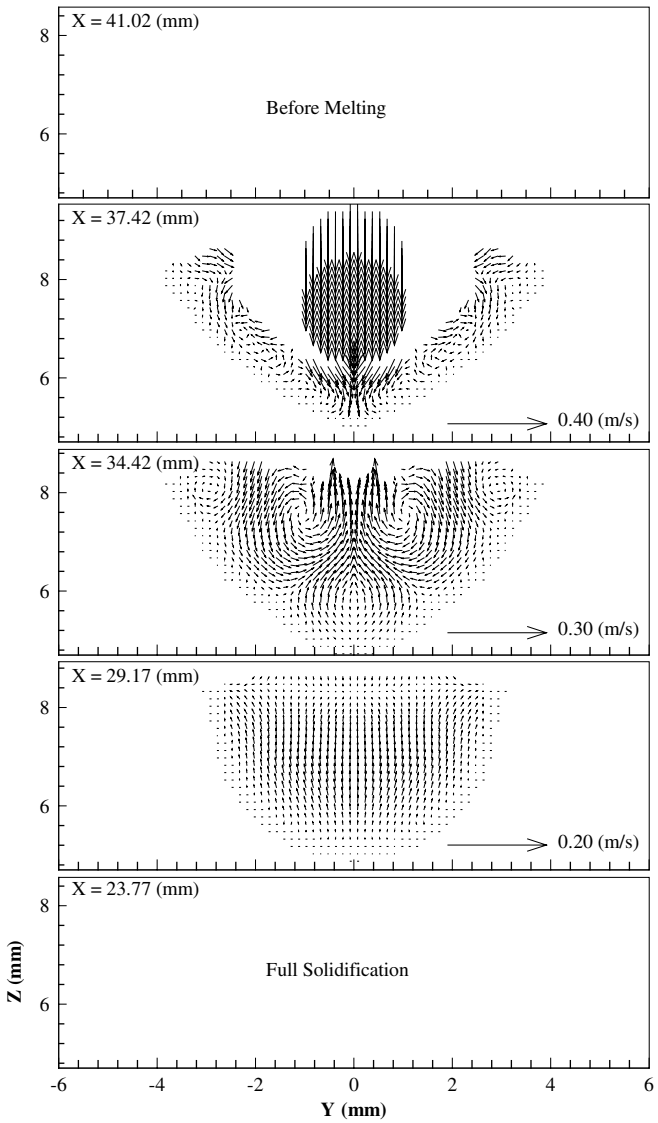

Figure 7. The corresponding velocity distribution as shown in figure 6.

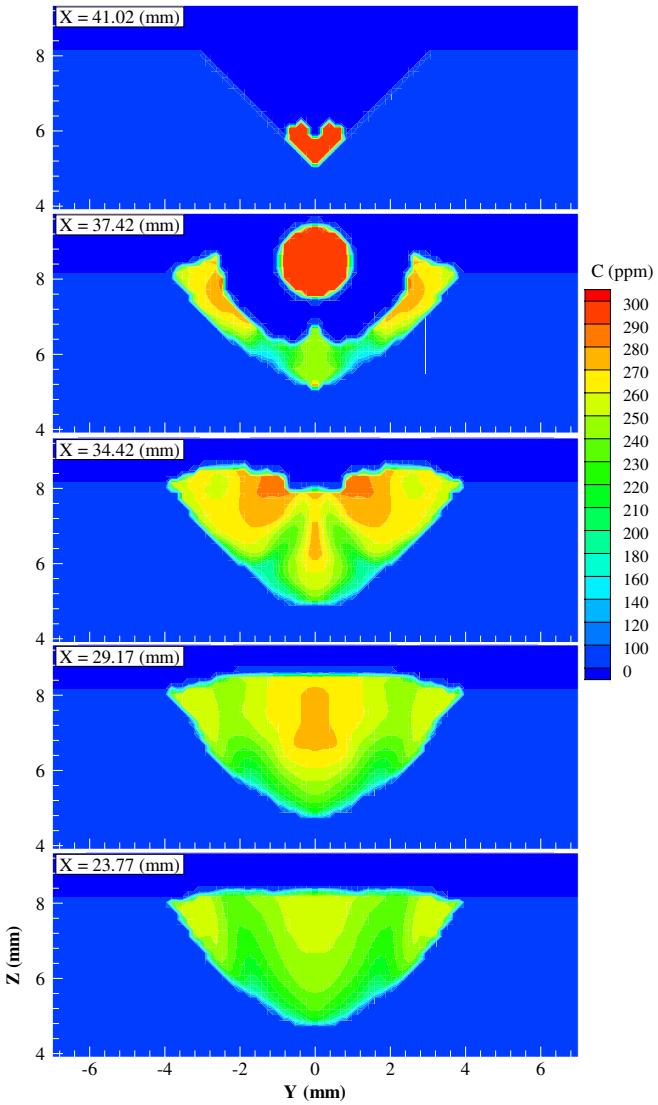

Figure 8. The corresponding sulfur concentration distribution as shown in figure 6.

explained in figure 3. The other is at the bottom of the groove due to the flow of droplet liquid along the groove bottom, as again shown in figure 3. As shown in figure 7, the fluid arising from the bottom of the groove comes from the flow along the bottom of the groove. Two vortices, one on each side of the groove, are created. At $X = 29.17$ mm, the maximum temperature occurs nearly at the centre of the groove, figure 6, as does the maximum sulfur concentration, figure 8. The flow in the groove is very small and is upwards, figure 7. At $X = 23.77$ mm, the weld pool is completely solidified, and the maximum temperature of the weld pool occurs near its top and in the centre. This is the final shape of the weld bead with the final sulfur distribution. As shown in figure 8, there are sulfur-lean stripes in the weld pool. The final sulfur distribution is not as uniform as compared with the case when there is no groove [15].

4.1.3. Three-dimensional view of the impinging process. Figure 9 is a partial view of the three-dimensional mesh system and velocity vectors at the top surface at $t = 4.309$ s. Figure 10 shows the corresponding top view of the velocity, temperature and concentration distributions. The weld pool is widest near the arc centre and decreases in width towards the rear part of the weld pool, as the weld pool loses heat to the base metal through conduction and convection and to its surroundings through convection and radiation.

The velocity distribution is very complicated, especially for the areas closest to the arc centre, which is impinged by the droplets. It will be easier to visualize the fluid flow in the entire weld pool by cross-referencing figures 4 (side view), 9 and 10. By comparing figure 4 with figure 10, it is clearly seen that the fluid in the 'bump' (figure 4) flows outwards and to the right and then meets with an opposing fluid flow on the left side. This leads to a V-shaped interface at which the fluid sinks to the bottom of the weld pool. The temperature distribution near the arc centre is complicated due to the mixing of droplets and the weld pool. It is noted that in addition to the energy carried by high temperature droplets, there is also an arc heat impacting on the top of the weld pool surface. As a result, the highest

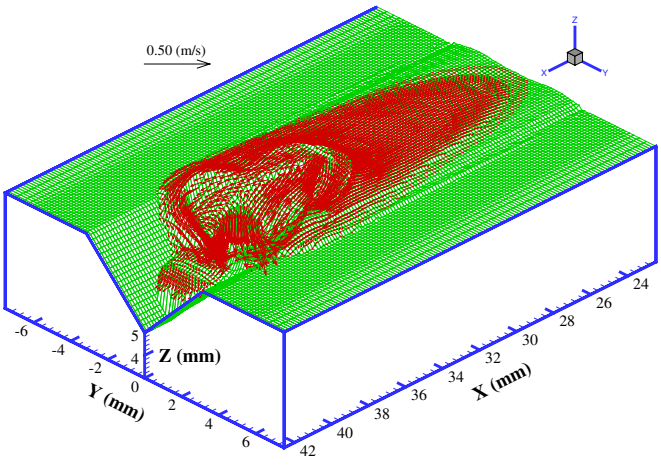

Figure 9. Partial view of a three-dimensional mesh system, weld bead shape and velocity distribution at $t = 4.309$ s.

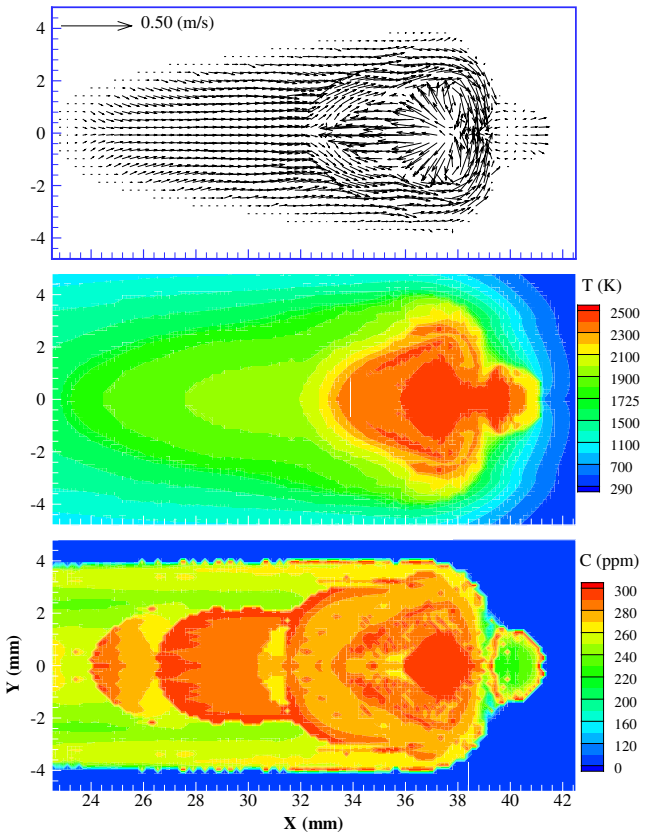

Figure 10. The corresponding top view of velocity, temperature and sulfur concentration distributions as shown in figure 9.

surface temperature occurs near the arc centre. However, the characteristics of surface sulfur distribution shown in figure 10 are quite different from those of the temperature distribution. The surface sulfur concentration distribution in the weld pool is directly related to the mixing between droplets and melted base metal. There are two spots with high sulfur concentration: one at the arc centre corresponding to the droplet and the other (between $X = 27$ mm and $X = 31$ mm) related to the ascending flow from the bottom of the groove, as shown in figure 4. The fluid consisting of this ascending flow is mainly from the droplets as discussed previously.

4.2. Effects of groove

Generally, the groove provides a 'confined channel' which facilitates the flow of filler metal along the bottom of the channel. The existence of the groove changes the fundamental flow pattern in the weld pool compared with the case without a groove [15]. As the groove tends to 'smooth' the fluid flow in the weld pool, it reduces the mixing between filler metal and melted base metal. Hence, in general, the uniformity of sulfur in the weld is not as good when there is a groove as compared with when there is no groove.

5. Conclusions

A mathematical model and associated numerical techniques have been developed to calculate the transient velocity, temperature and sulfur concentration distributions in the weld pool for a three-dimensional GMAW process for a thick plate with a groove. From the results of this study, it was found that the groove provides a confined channel facilitating the flow of filler metal along the bottom of the groove. This flow interacts with the flow caused by the surface tension force and the flow due to droplet impingement, leading to a large vortex in the weld pool. The V groove has a smooth effect so that the flow pattern is simpler than that without a groove. As a result, mixing between the filler metal and the weld pool is not good as compared with the case without a groove.

References

[1] 1983 *Welding, Brazing, and Soldering, Metals Handbook* vol 6, 9th edn (Metals Park, OH: American Society for Metals) pp 153–81
[2] Tsao M C and Wu C S 1988 *Weld. J.* **67** 70s
[3] Wang Y and Tsai H L 2001 *Int. J. Heat Mass Transfer* **44** 2067
[4] Fan H G and Kovacevic R 2004 *J. Phys. D: Appl. Phys.* **37** 2531
[5] Fan H G and Kovacevic R 1999 *Metall. Trans.* B **30** 791
[6] Wang Y and Tsai H L 2001 *Metall. Trans.* B **32** 501
[7] Zhu F L, Tsai H L, Marin S P and Wang P C 2004 *Prog. Comput. Fluid Dyn.* **4** 99
[8] Hu J and Tsai H L 2007 *Int. J. Heat Mass Transfer* **50** 833
[9] Hu J and Tsai H L 2007 *Int. J. Heat Mass Transfer* **50** 808
[10] Hu J and Tsai H L 2006 *J. Appl. Phys.* **100** 053304
[11] Hu J and Tsai H L 2007 *ASME J. Heat Transfer* **129** 1025
[12] Kim J W and Na S J 1994 *ASME J. Eng. Indus.* **116** 78
[13] Ushio M and Wu C S 1997 *Metall. Trans.* B **28** 509
[14] Cao Z, Yang Z and Chen X L 2004 *Weld. J.* **83** 169
[15] Hu J, Guo H and Tsai H L 2007 *Int. J. Heat Mass Transfer* at press, doi:10.1016/j.ijheatmasstransfer.2007.07.042
[16] Kothe D B and Mjolsness R C 1991 *Los Alamos Report* No LA-UR-91-2818
[17] Diao Q Z and Tsai H L 1993 *Metall. Trans.* A **24** 963
[18] Carman P C 1937 *Trans. Inst. Chem. Eng.* **15** 150
[19] Kubo K and Pehlke R D 1985 *Metall. Trans.* A **16** 823
[20] Beavers G S and Sparrow E M 1969 *J. Appl. Mech.* **36** 711
[21] Sahoo P, DeBroy T and Mcnallan M J 1988 *Metall. Trans.* B **19** 483
[22] Zacharia T, David S A and Vitek J M 1992 *Metall. Trans.* B **22** 233
[23] Welch J E, Harlow F H, Shannon J P and Daly B J 1966 *Los Alamos Report* No LA-3425
[24] Patankar S V 1980 *Numerical Heat Transfer and Fluid Flow* (New York: McGraw-Hill)
[25] Kerhaw D S 1978 *J. Comput. Phys.* **26** 43